Geochemical Perspectives Letters

Light calcium isotope anomaly in the Pitcairn mantle plume: a signal of pyroxenite melting

Y. Wang, Y.-S. He, O. Nebel, J.D. Woodhead

Supplementary Information

The Supplementary Information includes:

- 1. Ca Isotope Analysis Method
- 2. Radiogenic Ca Isotope Variation in Pitcairn Lavas
- 3. Modelling the Ca Isotope Composition of Melts in This Study
- Tables S-1 to S-10
- Figures S-1 to S-7
- Supplementary Information References

1. Ca Isotope Analysis Method

Calcium isotope analyses were performed at the Isotope Geochemistry Laboratory, China University of Geosciences, Beijing, following procedures detailed by He *et al.* (2017). Approximately 3 mg of powdered sample was dissolved in a concentrated HNO_3-HCl-HF mixture. One aliquot of the sample solutions, containing approximately 30 µg of Ca, was mixed with a ^{43}Ca-^{48}Ca double spike and then purified using AG50W-X12 resin (200–400 mesh, Bio-Rad). Isotope measurements were conducted using a Triton Plus thermal ionisation mass spectrometer (TIMS) equipped with customised L5 and H4 cups, allowing for static measurement of all Ca isotopes. Double Re filament assemblies were used, with approximately 5 µg of Ca loaded onto each evaporation filament. The ^{40}Ca signal intensity was approximately 15 V. Each analysis consisted of 120 cycles with an integration time of 16.776 s per cycle. Results are reported in δ notations relative to SRM915a, which was measured during each session:

$$\delta^{44/i}Ca\ (‰) = [(^{44}Ca/^{i}Ca)_{sample} / (^{44}Ca/^{i}Ca)_{SRM915a} - 1] \times 1000 \qquad \text{Eq. S-1}$$

where i represents 40 or 42. A secondary correction was applied using geological standard materials bracketing the unknown samples against their long-term values (Wang *et al.*, 2023). Radiogenic ^{40}Ca excess or deficit, expressed as ε values, was calculated from $\delta^{44/40}$Ca and $\delta^{44/42}$Ca values using the following equation:

$$\varepsilon^{40/44}\text{Ca} = (\delta^{44/42}\text{Ca} \times 2.0483 - \delta^{44/40}\text{Ca}) \times 10 \quad \text{Eq. S-2}$$

where the coefficient 2.0483 corresponds to the slope of mass-dependent fractionation in the exponential law (Farkaš *et al.*, 2011; He *et al.*, 2017). Multiple measurements were performed for each sample to improve precision, with means and 2 s.e. values reported (Table S-1). The long-term precision was ±0.03 ‰ and ±0.6 ε for $\delta^{44/42}$Ca and $\varepsilon^{40/44}$Ca, with each sample typically measured eight times (He *et al.*, 2017; Wang *et al.*, 2023). Measurements of reference materials SRM915b and BHVO-2 during this study yielded values consistent with those recommended in the literature (Table S-2).

2. Radiogenic Ca Isotope Variation in Pitcairn Lavas

The double spike technique used in this study allows the simultaneous, independent determination of $\delta^{44/40}$Ca and $\delta^{44/42}$Ca. Therefore, we can simultaneously get the sample's radiogenic Ca isotopic composition ($\varepsilon^{40/44}$Ca) using Eq. S-2 (He *et al.*, 2017). Overall, the Pitcairn lavas span $\varepsilon^{40/44}$Ca from −1.3 ± 0.5 to 0.4 ± 0.4 (typical analytical uncertainty ~ ±0.6 ε-units; Table S-1). The data separate systematically into two groups based on radiogenic Sr-Nd-Pb isotopic compositions (Fig. S-4a,b,c): (i) an EM1-like group comprising all Tedside samples + one seamount sample, with ^{87}Sr/^{86}Sr > 0.70448, ^{143}Nd/^{144}Nd < 0.512439, ^{206}Pb/^{204}Pb < 17.832, and a mean $\varepsilon^{40/44}$Ca = −0.1 ± 0.7 (2 s.d., n = 6), which is systematically higher than the BSE (from −1.2 to −0.6; Antonelli *et al.*, 2021; Wang *et al.*, 2024); and (ii) a more depleted/mid-ocean ridge basalt (MORB)-like group comprising six seamount samples + three post-erosional samples, averaging $\varepsilon^{40/44}$Ca = −0.8 ± 0.8 (2 s.d., n = 9), which is consistent with the BSE (Antonelli *et al.*, 2021; Wang *et al.*, 2024). A Student's t-test gives p = 0.006, indicating a statistically significant difference between the two groups (Fig. S-4d).

Given that seawater may strongly affect Sr isotopes but has only a weak influence on Nd isotopes (McCulloch *et al.*, 1981), the well-defined Sr-Nd isotopic coupling observed in the Pitcairn samples is unlikely to result from a single seawater-driven process and more likely reflects source-driven processes (*e.g.*, Woodhead *et al.*, 1993; Fig. S-1c). The EM1-like end member displays a higher radiogenic Ca isotope signature. Because of their low K/Ca (< 0.32) and young eruption ages (< 1 Ma) of Pitcairn lavas, any radiogenic ^{40}Ca growth over such timescales could be far below our analytical uncertainty. Thus, we consider post-eruptive in-situ ingrowth of ^{40}Ca to be negligible for the Tedside suite. Accordingly, the relatively higher $\varepsilon^{40/44}$Ca of Tedside samples compared with seamount samples most plausibly reflects source contributions from recycled materials, for example, carbonate-bearing recycled lithologies (and/or other enriched components), rather than seawater-driven processes.

Taken together, the radiogenic and stable Ca isotope data suggest that the contrasting behaviours of the Tedside and seamount lavas primarily reflect distinct lithologies in source. The seamount samples show mantle-like $\varepsilon^{40/44}$Ca but relatively light $\delta^{44/42}$Ca (Figs. S-2 and S-4), implying that their source contains only minor contributions from recycled surficial materials with $\varepsilon^{40/44}$Ca anomalies. Instead, their signatures are more consistent with a source dominated by recycled lower oceanic crust, whose incorporation into the ambient mantle forms secondary pyroxenite with lower $\delta^{44/42}$Ca, providing a plausible explanation for the lower $\delta^{44/42}$Ca of the seamount suite (Fig. 3). By contrast, the Tedside samples exhibit $\varepsilon^{40/44}$Ca slightly higher than the mantle (Fig. S-4), indicating a significant contribution from recycled surficial materials (*e.g.*, sedimentary carbonates), whereas their $\delta^{44/42}$Ca are close to MORB (Fig. S-2). This $\varepsilon^{40/44}$Ca-$\delta^{44/42}$Ca signature can be explained by two alternative scenarios: (i) the recycled carbonates entering the Pitcairn mantle source may have a relatively low Ca content. In that case, their large $\varepsilon^{40/44}$Ca difference may be sufficient to shift the bulk $\varepsilon^{40/44}$Ca of source, whereas any difference in their $\delta^{44/42}$Ca relative to the ambient mantle would have a negligible effect on the bulk $\delta^{44/42}$Ca to be resolved with our current analytical precision; and/or (ii) given the large and mantle-overlapping range of $\delta^{44/42}$Ca for sedimentary carbonates (Chen *et al.*, 2018), the recycled carbonate into the Pitcairn source may itself exhibit MORB-like $\delta^{44/42}$Ca, and therefore does not significantly shift the bulk $\delta^{44/42}$Ca of source. Future work will call on more high-precision stable and radiogenic Ca isotope data to further unravel the origin of Ca isotope variability in OIBs.

3. Modelling the Ca Isotope Composition of Melts in this Study

In this study, to explain the Ca isotope variation observed in Pitcairn basalts, we calculate the Ca isotopic composition of melts derived from the partial melting of eclogite, two types of secondary pyroxenite with varying garnet contents, garnet peridotite, and spinel peridotite. A non-modal batch melting model based on Williams and Bizimis (2014) is employed. The modelling results are summarised in Tables S-5 to S-10 below.

Firstly, we modelled the partial melting of spinel and garnet peridotite (Tables S-5 and S-6), as these two lithologies are considered representative of mantle sources without recycled components. However, the calculated trends of $\delta^{44/42}$Ca versus $(Dy/Yb)_N$ for these lithologies cannot explain the Pitcairn basalt data. For spinel peridotite (Table S-5), initial modal mode, melting mode, Ca partition coefficients (D_{Ca}), and bulk CaO content are taken from Workman and Hart (2005). Dy and Yb partition coefficients are from Salters and Stracke (2004). Contents of Dy and Yb are approximated as primitive mantle (Sun and McDonough, 1989). The initial $\delta^{44/42}$Ca of the mantle source is from Kang *et al.* (2017). Ca isotope fractionation factors between minerals and melt at 1000 K are taken from Antonelli *et al.* (2019) and Zhang *et al.* (2018), and then scaled to a magmatic temperature of 1673 K using a $1/T^2$ dependence (*i.e.* $\Delta^{44/42}Ca_{mineral\text{-}cpx}$ at

1673 K and $\Delta^{44/42}Ca_{melt\text{-}cpx}$ at 1673 K in Table S-5). These factors are widely accepted in the community for high-temperature Ca isotope modelling (*e.g.*, Soderman *et al.*, 2022). The calculated $\delta^{44/42}Ca$ of melt can be as low as 0.38 ‰ at very low degrees of melting, which clearly cannot account for the observed range in Pitcairn basalts (Fig. 3). We subsequently modelled the Ca isotopic composition of melts derived from garnet peridotite (Table S-6). Initial modal mode, melting mode, Ca partition coefficient, and bulk CaO are based on experimental studies of garnet peridotite melting (Davis *et al.*, 2011; Walter, 1998). Partition coefficients of Dy and Yb are taken from Salters *et al.* (2002). Contents of Dy and Yb, the $\delta^{44/42}Ca$ of mantle source, and Ca isotope fractionation factors are identical to those used in the spinel peridotite model (Sun and McDonough, 1989; Kang *et al.*, 2017; Zhang *et al.*, 2018; Antonelli *et al.*, 2019). The degree of melting ranges from 0 % to 22 % for spinel peridotite and from 0 % to 25 % for garnet peridotite, constrained by the near exhaustion of residual clinopyroxene. The lowest calculated $\delta^{44/42}Ca$ of the melt is 0.37 ‰, which still cannot reproduce the range observed in Pitcairn basalts (Fig. 3).

Next, we investigate high pressure eclogite-derived melts (referred to as HPEM in the main text), generated by the partial melting of recycled MORB at high pressure. The modelling procedure and results for HPEM are presented in Table S-7. The initial modal and melting modes are adopted from Sobolev *et al.* (2000), which simulate partial melting of eclogite derived from recycled crustal components at high pressure. Recycled oceanic crust transforms into silica-saturated eclogite under mantle P-T conditions, with high-pressure eclogites containing abundant garnet (Thomson *et al.*, 2016), facilitating the generation of Ca-isotopically light melts (Wang *et al.*, 2019). Mineral CaO contents and Ca partition coefficients between minerals and melt are based on the compositions of silicate melts and residual minerals obtained from high P-T experiments (3–5.1 GPa) on the partial melting of recycled MORB (Thomson *et al.*, 2016). Dy and Yb partition coefficients are from Sobolev *et al.* (2000). The bulk CaO content of the eclogite (10.06 wt. %) is calculated from modal mineralogy and partition coefficients, consistent with the average MORB value (11.39 wt. %; Arevalo and McDonough, 2010). Dy and Yb contents of the eclogite are from Arevalo and McDonough (2010), and its initial $\delta^{44/42}Ca$ is assumed to be the mean $\delta^{44/42}Ca$ of MORBs (Eriksen and Jacobsen, 2022). Ca isotope fractionation factors between minerals and melt are identical to those used for modelling peridotite melting (Antonelli *et al.*, 2019; Zhang *et al.*, 2018). We acknowledge that the calculated $\delta^{44/42}Ca$ of HPEM could be a maximum estimate, particularly if jadeite-rich clinopyroxene is also enriched in heavy Ca isotopes (Wang *et al.*, 2019). The degree of melting for recycled MORB ranges from 1 % to 34 %, until the exhaustion of residual coesite. These melts exhibit substantially light Ca isotope compositions due to abundant garnet proportion in the residue. However, the $(Dy/Yb)_N$ range of the HPEM is relatively narrow and does not fall within the range observed in Pitcairn basalts (Fig. 3).

We then consider a three-step model involving the formation and melting of secondary pyroxenites. Recycled oceanic crust is preferentially melted during mantle adiabatic upwelling (Ringwood and Green, 1966), and the resulting silica-

rich melts react with ambient peridotite to form secondary pyroxenite (Yaxley and Green, 1998; Sobolev *et al.*, 2000, 2005). Melting of secondary pyroxenite with abundant garnet in the residue can produce Ca-isotopically light melts (Wang *et al.*, 2019). Similar models have been widely applied to explain the origin of OIBs, including reproducing the trace element compositions of Pitcairn-Gambier OIBs (Delavault *et al.*, 2015), interpreting the characteristics of melt inclusions in Mauna Loa basalts with high Sr and low REE contents, and high Sr/Ce ratios (Sobolev *et al.*, 2000), as well as the high Ni and SiO_2 contents observed in Hawaiian shield-stage basalts (Sobolev *et al.*, 2005):

1. Generation of HPEM. As described above, recycled oceanic crust was modelled to undergo partial melting at ~30 %, producing eclogitic melts (Table S-7).

2. Formation of secondary pyroxenites. A binary mixing model is applied to estimate the trace element and Ca isotopic compositions of secondary pyroxenites (Table S-8). The recycled oceanic crust component is represented by the HPEM in Step 1, while the peridotite component is assumed to be depleted mantle (Salters and Stracke, 2004) with a Ca isotopic composition from Kang *et al.* (2017). Two scenarios are considered here: Secondary pyroxenite 1 comprises 5 % HPEM and 95 % peridotite, representing a garnet bearing lithology formed at relatively low pressure from upper oceanic crust-derived melts. The 5 % HPEM proportion is taken from the estimate obtained when evaluating the trace element compositions of the extreme EM-1 end member samples on Gambier Island in the Pitcairn chain (Delavault *et al.*, 2015), which suggests a source containing 5 % recycled oceanic crust and 95 % peridotite. Secondary pyroxenite 2 comprises 50 % HPEM and 50 % peridotite, representing a garnet-rich lithology formed at higher pressure from lower oceanic crust-derived melts. These assumptions are supported by mineral proportions observed in both modelling and experimental studies for reaction pyroxenites. Secondary pyroxenite formed by reaction between peridotite and melt derived from an eclogitised oceanic basalt at 3.5 GPa and 1350 °C contains 15.5 % garnet (Sobolev *et al.*, 2005), and experimental secondary pyroxenite formed at 3 GPa and 1475 °C contains ~10 % garnet (Tuff and Gibson, 2007). In contrast, secondary pyroxenite formed by reaction between peridotite and melt derived from eclogitised oceanic gabbro at 4.5 GPa and 1525 °C contains 24.3 % garnet (Sobolev *et al.*, 2005), and experimental secondary pyroxenite formed at 5 GPa and 1600 °C contains ~25 % garnet (Tuff and Gibson, 2007).

3. Partial melting of secondary pyroxenites. Melts derived from secondary pyroxenites 1 and 2 were modelled using a non-modal batch melting approach, with the results presented in Tables S-9 and S-10, respectively. The initial garnet proportion in secondary pyroxenite 1 is set at 10 %, and that in secondary pyroxenite 2 set at 24.3 % (Sobolev *et al.*, 2005; Tuff and Gibson, 2007), considering their distinct HPEM proportions. The melting mode follows Delavault *et al.* (2015). Ca partition coefficient is from Yaxley and Green (1998), and Dy and Yb partition

coefficients are from Pertermann *et al.* (2004). Bulk CaO, Dy, Yb contents and $\delta^{44/42}$Ca value are taken from Step 2 calculations. Ca isotope fractionation factors are the same as those used in Tables S-5 to S-7. The degree of melting ranges from 0 % to 21 % for secondary pyroxenite 1 and from 0 % to 50 % for secondary pyroxenite 2, constrained by the exhaustion of residual garnet.

The modelling results demonstrate that partial melting of secondary pyroxenite 2 can generate melts with $\delta^{44/42}$Ca values as low as those observed in the isotopically lightest Pitcairn basalts (Table S-10), and can effectively reproduce the $(Dy/Yb)_N$ variations of the Pitcairn samples (Fig. 3a). Meanwhile, melts derived from secondary pyroxenite 1 can also account for the MORB-like Ca isotope compositions observed in the Tedside samples. Given the extreme EM-1 end member trace element and radiogenic isotope characteristics of the Tedside lavas, we suggest that this pyroxenitic source is the primary contributor to their Ca isotope signatures, rather than a simple garnet peridotite source (Fig. 3a).

We further modelled the variations in stable Ca isotopic compositions and radiogenic isotopic ratios (*e.g.*, $^{87}Sr/^{86}Sr$) (Fig. 3b). To reproduce the enriched $^{87}Sr/^{86}Sr$ of Tedside lavas, carbonate bearing sediments were added to the source of HPEM (*i.e.* recycled oceanic crust). Firstly, a simple binary mixing approach was used to evaluate the effect of sediment addition. Carbonate-bearing sediments were added to recycled oceanic crust to generate the HPEM component. The recycled oceanic crust was assumed to have Sr = 130 ppm, CaO = 11.4 wt. %, $^{87}Sr/^{86}Sr$ = 0.704250 (White and Klein, 2014), and $\delta^{44/42}$Ca = 0.39 ‰ (Eriksen and Jacobsen, 2022). The carbonate-bearing sediment component was assumed to have CaO = 40 wt. % with $\delta^{44/42}$Ca = 0.29 ‰, and Sr = 1151 ppm with $^{87}Sr/^{86}Sr$ = 0.70880 (Fantle and Tipper, 2014; Huang and Xiao, 2016). The calcium carbonate composition is adopted here to approach the scenario, in which Ca isotope systematics of the hybridised source might have been influenced the most by addition of sediments. Based on the Ca isotope fractionation associated with high-pressure melting of recycled oceanic crust (~0.07 ‰; Table S-7), and assuming that $^{87}Sr/^{86}Sr$ remain unchanged during partial melting, we calculated the variations in $\delta^{44/42}$Ca and $^{87}Sr/^{86}Sr$ for melts derived from mixtures of recycled oceanic crust and carbonate-bearing sediments. The results are illustrated by the blue dashed line in Figure 3b. Because carbonate-bearing sediments have much higher Sr concentrations and higher $^{87}Sr/^{86}Sr$ than oceanic crust, the addition of small amounts of sediment significantly shifts the $^{87}Sr/^{86}Sr$ of the melt. In contrast, the effect on $\delta^{44/42}$Ca is limited due to relatively smaller difference in CaO contents and Ca isotopic compositions between sediments and oceanic crust. For example, the addition of 5 % carbonate-bearing sediments lowers the melt $\delta^{44/42}$Ca by only ~0.02 ‰ (Fig. 3b), which is much smaller than the Ca isotope fractionation generated during partial melting of recycled oceanic crust (~0.07 ‰, Table S-7).

We then modelled the formation of secondary pyroxenites through interaction between HPEM and ambient mantle peridotite using the same binary mixing approach as applied in Figure 3a. The mantle peridotite was assumed to contain

10 ppm Sr with $^{87}Sr/^{86}Sr$ = 0.70330 (Sobolev *et al.*, 2005), and 3.55 wt. % CaO with $\delta^{44/42}Ca$ = 0.42 ‰ (Kang *et al.*, 2017). The HPEM was assumed to contain 300 ppm Sr with $^{87}Sr/^{86}Sr$ = 0.70425 (Sobolev *et al.*, 2005), and 11.4 wt. % CaO with $\delta^{44/42}Ca$ = 0.32 ‰ corresponding to the HPEM composition estimated in this study (Table S-7). Specifically, to reproduce the enriched $^{87}Sr/^{86}Sr$ of the Tedside lavas, 5 % carbonate-bearing sediments were added to recycled oceanic crust to generate HPEM containing 5 % sediments. The Sr and Ca isotopic compositions of this HPEM component were taken from the calculation described above (blue dashed line in Fig. 3b). The calculated mixing relationships between HPEM and mantle peridotite are shown as two grey dashed lines in Figure 3b. Secondary pyroxenite 1 was generated from 5 % HPEM (with 5 % sediment added to its source) + 95 % ambient peridotite, whereas secondary pyroxenite 2 was generated from 50 % HPEM + 50 % ambient peridotite, consistent with the calculation in Figure 3a (*i.e.* the grey dashed line in Fig. 3a). The presence or absence of sediment components is consistent with the general understanding of how sediments are carried by subducting oceanic crust, with the upper oceanic crust typically incorporating more sediments than the lower crust. Partial melting of these secondary pyroxenites (illustrated by white arrows in Fig. 3b) can reproduce the observed Ca isotope variations in Pitcairn lavas (Fig. 3b). These results suggest that the Ca isotope variations are primarily controlled by the proportion of recycled oceanic crust-derived HPEM in the Pitcairn mantle plume and by Ca isotope fractionation associated with subsequent partial melting. In contrast, the addition of carbonate-bearing sediments is mainly required to reproduce the enriched radiogenic isotope signatures of the EM-1 component and has only a limited effect on Ca isotopes, consistent with the observation that the most enriched samples display MORB-like $\delta^{44/42}Ca$ values.

The $\delta^{44/42}Ca$ range observed in Pitcairn basalts in this study is broadly consistent with global OIBs, and their REE compositions are comparable to those of the isotopically lightest OIB samples from other hotspots (Eriksen *et al.*, 2024; Eriksen and Jacobsen, 2022). Notably, OIB samples with the highest $(Dy/Yb)_N$ do not exhibit the lightest Ca isotope compositions. Although the mechanism by which recycled oceanic crust components influence Ca isotopic compositions in OIBs from other hotspots remains unclear, the secondary pyroxenite partial melting model proposed in this study may offer a new explanation for the observed relationship between $\delta^{44/42}Ca$ and $(Dy/Yb)_N$ in global OIBs. According to our model, partial melting of secondary pyroxenites with variable garnet proportions can account for the variations observed in $\delta^{44/42}Ca$ versus $(Dy/Yb)_N$ (Fig. 4). Here, the composition of secondary pyroxenite is modelled as a binary mixing between mantle peridotite and HPEM in varying proportions. As shown by the black grid in Figure 4, vertical lines represent the proportion of HPEM involved in secondary pyroxenite formation (ranging from 0 % to 100 %), with the remaining proportion being mantle peridotite. Horizontal lines represent the degree of partial melting of the secondary pyroxenite (from 20 % to 60 %). Given that secondary pyroxenites formed from different proportions of HPEM are expected to have distinct modal abundances of garnet and clinopyroxene, they may therefore undergo melting under different conditions. Nevertheless, for the sake of model simplicity and comparability, we adopted the same

melting parameters as those used in Figure 3 and Tables S-9 and S-10. The results show that secondary pyroxenites formed from high proportions of HPEM (*i.e.* with higher garnet proportions) undergoing varying degrees of partial melting reproduce the Ca isotope variation observed in OIBs (Fig. 4). Given that previous studies have demonstrated significant contributions of secondary pyroxenite in some hotspot magmas (*e.g.*, >80 % in Koolau, Hawaii; Sobolev *et al.*, 2005), partial melting of secondary pyroxenites may provide a new perspective for interpreting Ca isotope anomalies at other hotspots.

Supplementary Tables

Tables S-1 to S-10 (.xlsx) are available for download from the online version of this article at https://doi.org/10.7185/geochemlet.2613

Table S-1 Calcium isotopic compositions for Pitcairn Island and seamount basalts.

a. 2 s.e. denotes two standard errors of the mean, 2 s.e. = 2s.d./sqrt(n).

b. $\varepsilon^{40/44}$Ca is calculated from independently obtained $\delta^{44/42}$Ca and $\delta^{44/40}$Ca, following the method of Farkaš *et al.* (2011).

c. n denotes number of analyses of Ca isotopes.

Table S-2 Calcium isotopic compositions of standard materials.

a. Reference sources: Zhu *et al.* (2020); Dai *et al.* (2022); Eriksen and Jacobsen (2022).

b. 2 s.d. denotes two standard deviations.

c. n denotes number of analyses of Ca isotopes.

Table S-3 Major and trace element concentrations for Pitcairn Island and seamount basalts. Major and trace element concentration data are from Woodhead and McCulloch (1989) and Woodhead and Devey (1993).

Table S-4 Trace element concentrations corrected for the olivine accumulation for Pitcairn Island and seamount basalts. Trace element concentrations (Woodhead and McCulloch, 1989; Woodhead and Devey, 1993) are corrected for the olivine accumulation to 9.5 wt. % MgO. Three evolved samples with MgO < 3.8 wt. % (denoted by *) were excluded from this correction. Partition coefficients used in the correction are from Bédard (2005).

Table S-5 Calcium isotopic compositions of spinel peridotite melt.

Parameters sources: a. Workman and Hart (2005); b. Salters and Stracke (2004); c. Antonelli *et al.* (2019); d. Zhang *et al.* (2018); e. Sun and McDonough (1989); f. Kang *et al.* (2017). g. The subscript N denotes normalisation of residual phases to 100 %.

Table S-6 Calcium isotopic compositions of garnet peridotite melt.

Parameters sources: a. Davis et al. (2011); b. Walter (1998); c. Salters and Stracke (2004); d. Antonelli *et al.* (2019); e. Zhang *et al.* (2018); f. Sun and McDonough (1989); g. Kang *et al.* (2017). h. The subscript N denotes normalisation of residual phases to 100 %.

Table S-7 Calcium isotopic compositions of high pressure eclogite-derived melt (HPEM).

Parameters sources: a. Sobolev *et al.* (2000); b. Thomson *et al.* (2016); c. Antonelli *et al.* (2019); d. Zhang *et al.* (2018); e. Arevalo and McDonough (2010); f. Eriksen and Jacobsen (2022). g. The subscript N denotes normalisation of residual phases to 100 %.

Table S-8 Formation models for two types of secondary pyroxenite.

a. HPEM = high pressure eclogite-derived melt, and its composition corresponds to the 30 % partial melting result in Table S-7.

b. PM = primitive mantle (Sun and McDonough, 1989).

Table S-9 Calcium isotopic compositions of melt from secondary pyroxenite 1.

Parameters sources: a. Sobolev *et al.* (2005); b. Delavault *et al.* (2015); c. Table S-8; d. Yaxley and Green (1998); e. Pertermann *et al.* (2004); f. Antonelli *et al.* (2019); g. Zhang *et al.* (2018). h. The subscript N denotes normalisation of residual phases to 100 %.

Table S-10 Calcium isotopic compositions of melt from secondary pyroxenite 2.

Parameters sources: a. Sobolev *et al.* (2005); b. Delavault *et al.* (2015); c. Table S-8; d. Yaxley and Green (1998); e. Pertermann *et al.* (2004); f. Antonelli *et al.* (2019); g. Zhang *et al.* (2018). h. The subscript N denotes normalisation of residual phases to 100 %.

Supplementary Figures

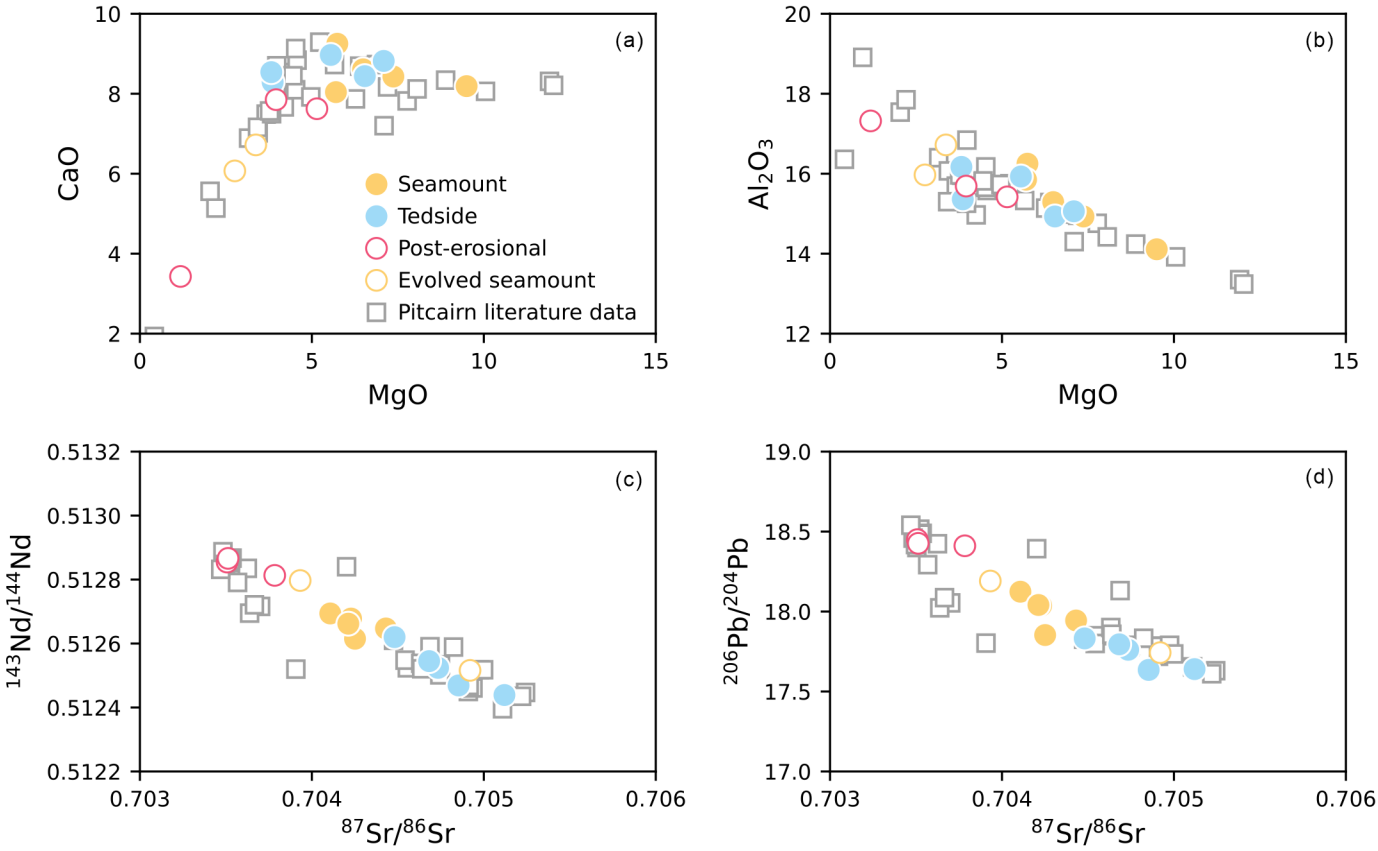

Figure S-1 **(a)** CaO *vs.* MgO, **(b)** Al_2O_3 *vs.* MgO, **(c)** $^{143}Nd/^{144}Nd$ *vs.* $^{87}Sr/^{86}Sr$, **(d)** $^{206}Pb/^{204}Pb$ *vs.* $^{87}Sr/^{86}Sr$ for Pitcairn basalts. Pitcairn basalt data are taken from the GEOROC database (http://georoc.eu/).

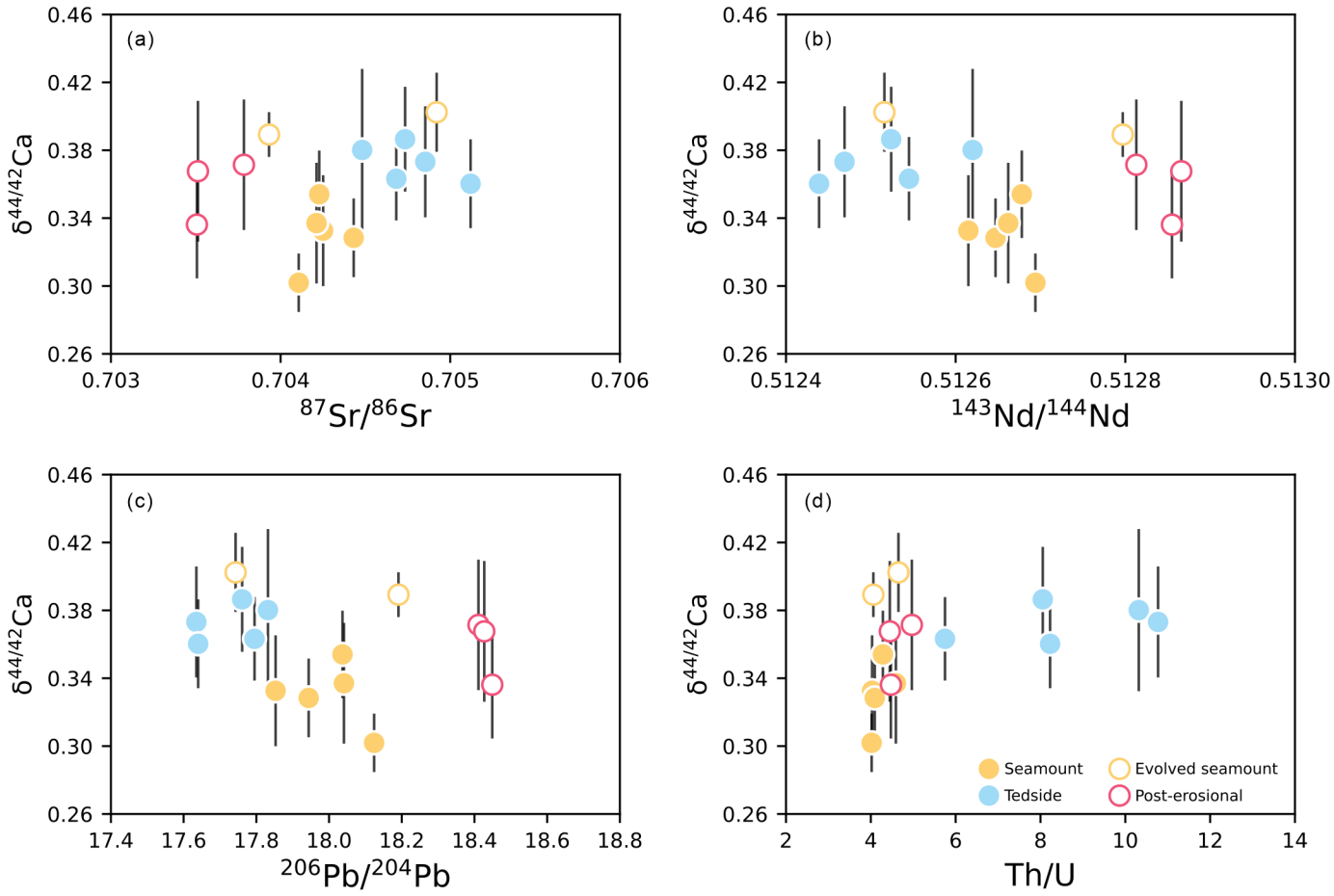

Figure S-2 $\delta^{44/42}$Ca *vs.* **(a)** ^{87}Sr/^{86}Sr, **(b)** ^{143}Nd/^{144}Nd, **(c)** ^{206}Pb/^{204}Pb and **(d)** Th/U for Pitcairn basalts. Typical 2 s.e. for $\varepsilon^{40/44}$Ca and $\delta^{44/42}$Ca are ±0.03 ‰ and ±0.6 ε, respectively. Hollow symbols denote evolved samples with MgO < 3.8 wt. %. Trace elemental and isotopic data are from Woodhead and McCulloch (1989) and Woodhead and Devey (1993). Trace element data for Pitcairn basalts were corrected for the influence of olivine accumulation, following Nebel *et al.* (2019), except for samples with MgO < 3.8 wt. % due to the unavailability of an effective correction method for clinopyroxene fractionation.

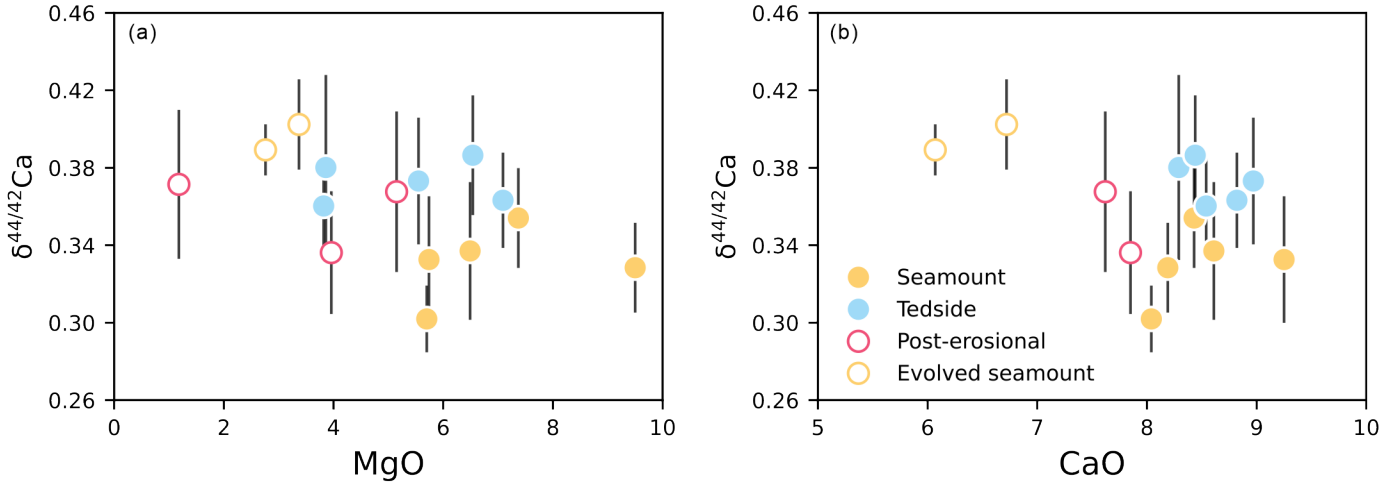

Figure S-3 $\delta^{44/42}$Ca *vs.* **(a)** MgO and **(b)** CaO for Pitcairn basalts.

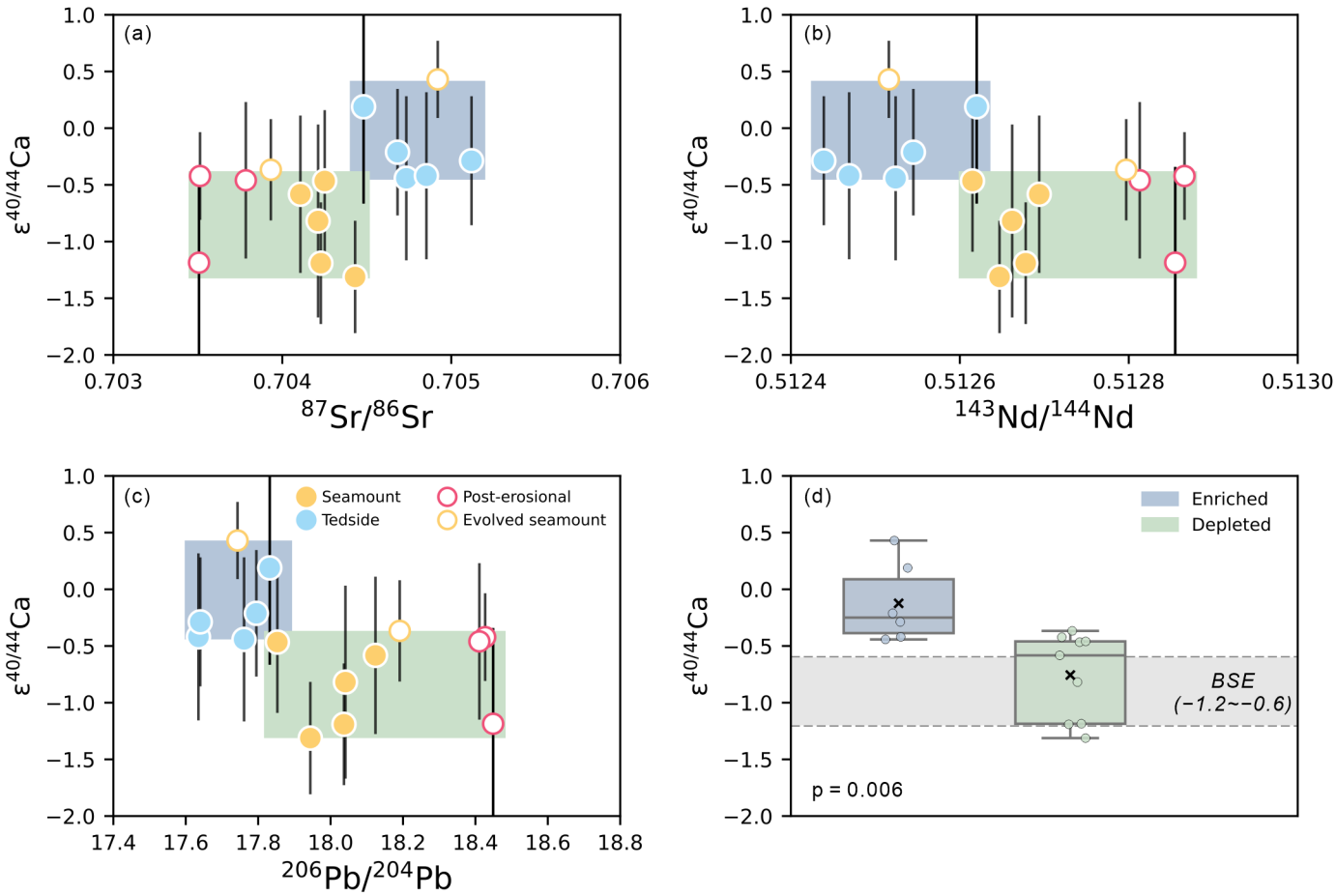

Figure S-4 $\varepsilon^{40/44}$Ca *vs.* **(a)** $^{87}Sr/^{86}Sr$, **(b)** $^{143}Nd/^{144}Nd$, and **(c)** $^{206}Pb/^{204}Pb$ for Pitcairn lavas, and **(d)** a two-sample t-test

for relatively enriched and depleted groups of Pitcairn lavas, which gives p = 0.006, indicating a significant difference between the enriched and depleted groups.

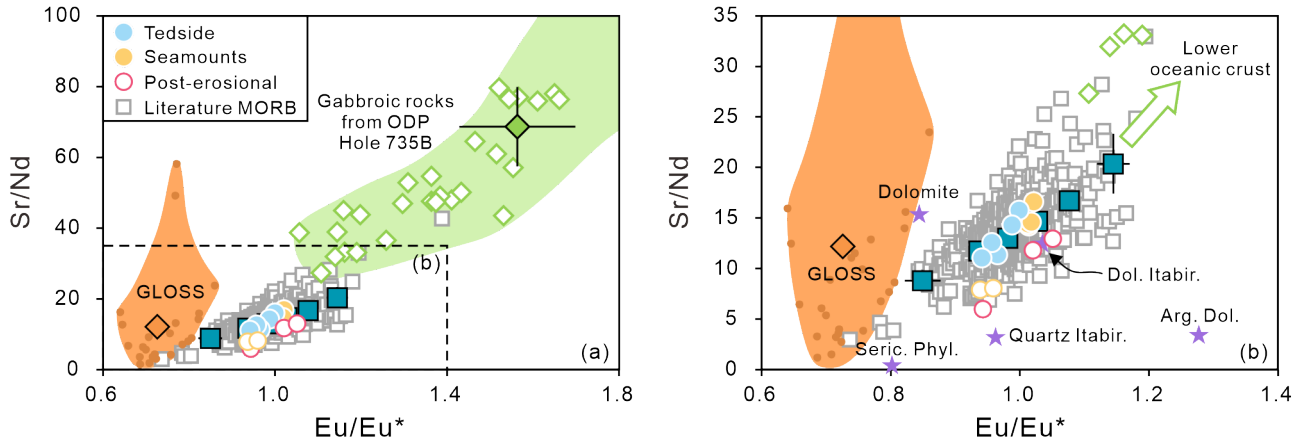

Figure S-5 Sr/Nd *vs.* Eu/Eu* for Pitcairn basalts, with MORB, GLOSS, and gabbroic rock data for comparison. MORB data are from Arevalo and McDonough (2010). The data have been categorised into six groups based on Eu/Eu* values: ≤ 0.90, 0.90–0.95, *etc*. Grey squares denote mean values of MORB corresponding to six segments of data based on Eu/Eu*. The orange region represents the sediment columns subducting at different trenches, with the orange rhombus indicating the mean GLOSS composition (Plank and Langmuir, 1998). Green hollow rhombuses represent gabbroic rocks from ODP Hole 735B (Bach *et al.*, 2001), and the green solid symbol indicates the mean value of these gabbroic rocks, representing lower oceanic crust. Purple pentagrams in panel (b) indicate possible terrestrial and marine sediment components (Spier *et al.*, 2007). Abbreviations: Seric. Phyl. — Sericitic phyllite; Arg. Dol. — Argillaceous dolomite; Dol. Itabir. — Dolomitic itabirite; Quartz Itabir. — Quartz itabirite.

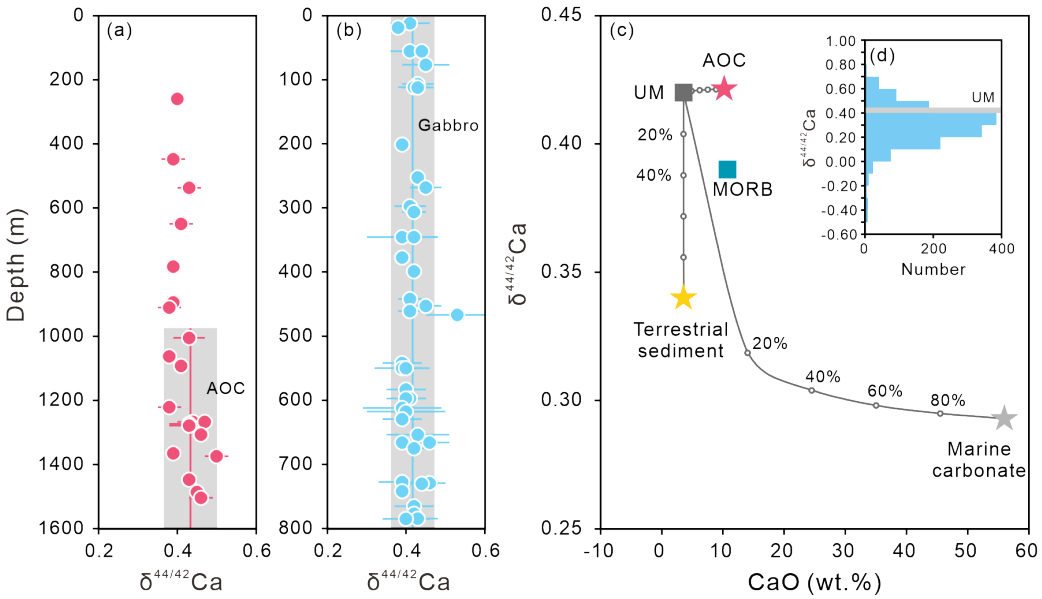

Figure S-6 **(a)** $\delta^{44/42}$Ca for altered oceanic crustal rocks, **(b)** $\delta^{44/42}$Ca for gabbros, **(c)** mixing lines between the upper mantle and different recycled materials, and **(d)** $\delta^{44/42}$Ca for marine carbonates. Altered oceanic crust and gabbro samples are from IODP Site 1256 and Hole U1473A, respectively. Sources for $\delta^{44/42}$Ca of end members in panel (c): AOC—the mean value for altered oceanic crustal rocks; terrestrial sediment—assumed to be equivalent to the upper continental crust; marine carbonates—the mean value based on previously reported data (Fantle and Tipper, 2014).

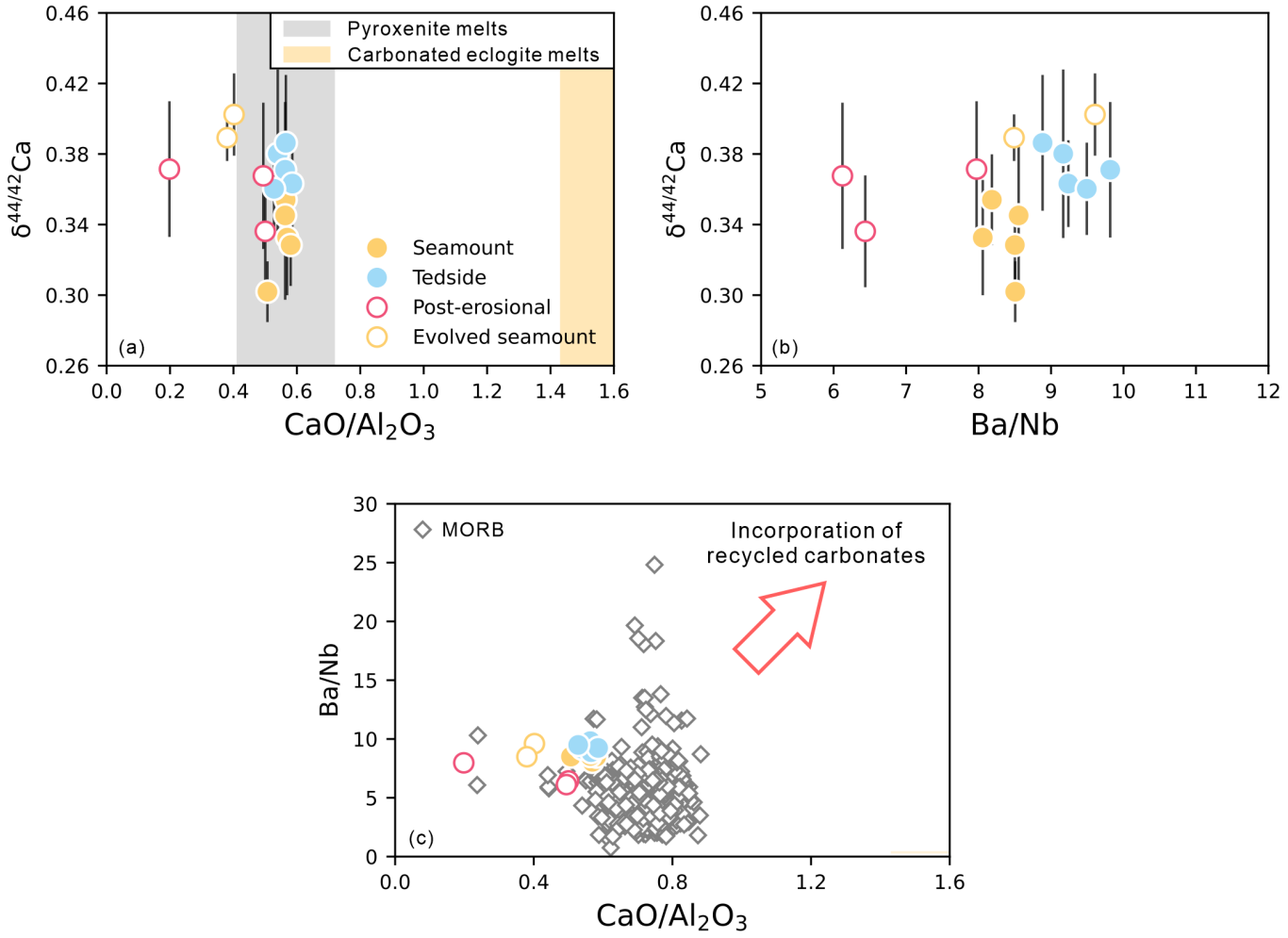

Figure S-7 (a) $\delta^{44/42}$Ca *vs.* CaO/Al_2O_3, **(b)** $\delta^{44/42}$Ca *vs.* Ba/Nb, and **(c)** Ba/Nb *vs.* CaO/Al_2O_3. Grey and yellow shaded regions in panel (a) represent experimental pyroxenite melts (Pertermann and Hirschmann, 2003) and carbonated eclogite melts (Dasgupta *et al.*, 2006), respectively. Hollow diamonds in panel (c) represent literature MORB data (Arevalo and McDonough, 2010).

Supplementary Information References

Antonelli, M.A., DePaolo, D.J., Christensen, J.N., Wotzlaw, J.-F., Pester, N.J., Bachmann, O. (2021) Radiogenic ^{40}Ca in Seawater: Implications for Modern and Ancient Ca Cycles. *ACS Earth and Space Chemistry* 5, 2481–2492. https://doi.org/10.1021/acsearthspacechem.1c00179

Antonelli, M.A., Schiller, M., Schauble, E.A., Mittal, T., DePaolo, D.J., Chacko, T., Grew, E.S., Tripoli, B. (2019) Kinetic and equilibrium Ca isotope effects in high-T rocks and minerals. *Earth and Planetary Science Letters* 517, 71–82. https://doi.org/10.1016/j.epsl.2019.04.013

Arevalo, R., McDonough, W.F. (2010) Chemical variations and regional diversity observed in MORB. *Chemical Geology* 271, 70–85. https://doi.org/10.1016/j.chemgeo.2009.12.013

Bach, W., Alt, J.C., Niu, Y., Humphris, S.E., Erzinger, J., Dick, H.J.B. (2001) The geochemical consequences of late-stage low-grade alteration of lower ocean crust at the SW Indian Ridge: results from ODP Hole 735B (Leg 176). *Geochimica et Cosmochimica Acta* 65, 3267–3287. https://doi.org/10.1016/S0016-7037(01)00677-9

Bédard, J.H. (2005) Partitioning coefficients between olivine and silicate melts. *Lithos* 83, 394–419. https://doi.org/10.1016/j.lithos.2005.03.011

Chen, C., Liu, Y., Feng, L., Foley, S.F., Zhou, L., Ducea, M.N., Hu, Z. (2018) Calcium isotope evidence for subduction-enriched lithospheric mantle under the northern North China Craton. *Geochimica et Cosmochimica Acta* 238, 55–67. https://doi.org/10.1016/j.gca.2018.06.038

Dai, W., Moynier, F., Paquet, M., Moureau, J., Debret, B., Siebert, J., Gerard, Y., Zhao, Y. (2022) Calcium isotope measurements using a collision cell (CC)-MC-ICP-MS. *Chemical Geology* 590, 120688. https://doi.org/10.1016/j.chemgeo.2021.120688

Dasgupta, R., Hirschmann, M.M., Stalker, K. (2006) Immiscible Transition from Carbonate-rich to Silicate-rich Melts in the 3 GPa Melting Interval of Eclogite + CO_2 and Genesis of Silica-undersaturated Ocean Island Lavas. *Journal of Petrology* 47, 647–671. https://doi.org/10.1093/petrology/egi088

Davis, F.A., Hirschmann, M.M., Humayun, M. (2011) The composition of the incipient partial melt of garnet peridotite at 3 GPa and the origin of OIB. *Earth and Planetary Science Letters* 308, 380–390. https://doi.org/10.1016/j.epsl.2011.06.008

Delavault, H., Chauvel, C., Sobolev, A., Batanova, V. (2015) Combined petrological, geochemical and isotopic modeling of a plume source: Example of Gambier Island, Pitcairn chain. *Earth and Planetary Science Letters* 426, 23–35. https://doi.org/10.1016/j.epsl.2015.06.013

Delavault, H., Chauvel, C., Thomassot, E., Devey, C.W., Dazas, B. (2016) Sulfur and lead isotopic evidence of relic Archean sediments in the Pitcairn mantle plume. *Proceedings of the National Academy of Sciences* 113, 12952–12956. https://doi.org/10.1073/pnas.1523805113

Eriksen, Z.T., Jacobsen, S.B. (2022) Calcium isotope constraints on OIB and MORB petrogenesis: The importance of melt mixing. *Earth and Planetary Science Letters* 593, 117665. https://doi.org/10.1016/j.epsl.2022.117665

Eriksen, Z.T., Jacobsen, S.B., Day, J.M.D., White, W.M. (2024) Calcium isotope variability among ocean islands reveals the physical and lithological controls on mantle partial melting. *Geochimica et Cosmochimica Acta*. https://doi.org/10.1016/j.gca.2024.02.011

Fantle, M.S., Tipper, E.T. (2014) Calcium isotopes in the global biogeochemical Ca cycle: Implications for development of a Ca isotope proxy. *Earth-Science Reviews* 129, 148–177. https://doi.org/10.1016/j.earscirev.2013.10.004

Farkaš, J., Déjeant, A., Novák, M., Jacobsen, S.B. (2011) Calcium isotope constraints on the uptake and sources of Ca^{2+} in a base-poor forest: A new concept of combining stable ($\delta^{44/42}Ca$) and radiogenic (εCa) signals. *Geochimica et Cosmochimica Acta* 75, 7031–7046. https://doi.org/10.1016/j.gca.2011.09.021

He, Y., Wang, Y., Zhu, C., Huang, S., Li, S. (2017) Mass-Independent and Mass-Dependent Ca Isotopic Compositions of Thirteen Geological Reference Materials Measured by Thermal Ionisation Mass Spectrometry. *Geostandards and Geoanalytical Research* 41, 283–302. https://doi.org/10.1111/ggr.12153

Huang, J., Xiao, Y. (2016) Mg-Sr isotopes of low-$\delta^{26}Mg$ basalts tracing recycled carbonate species: Implication for the initial melting depth of the carbonated mantle in Eastern China. *International Geology Review* 58, 1350–1362. https://doi.org/10.1080/00206814.2016.1157709

Kang, J.-T., Ionov, D.A., Liu, F., Zhang, C.-L., Golovin, A.V., Qin, L.-P., Zhang, Z.-F., Huang, F. (2017) Calcium isotopic fractionation in mantle peridotites by melting and metasomatism and Ca isotope composition of the Bulk Silicate Earth. *Earth and Planetary Science Letters* 474, 128–137. https://doi.org/10.1016/j.epsl.2017.05.035

McCulloch, M.T., Gregory, R.T., Wasserburg, G.J., Taylor, H.P. (1981) Sm-Nd, Rb-Sr, and^{18} O/^{16} O isotopic systematics in an oceanic crustal section: Evidence from the Samail Ophiolite. *Journal of Geophysical Research: Solid Earth* 86, 2721–2735. https://doi.org/10.1029/JB086iB04p02721

Nebel, O., Sossi, P.A., Bénard, A., Arculus, R.J., Yaxley, G.M., Woodhead, J.D., Rhodri Davies, D., Ruttor, S. (2019) Reconciling petrological and isotopic mixing mechanisms in the Pitcairn mantle plume using stable Fe isotopes. *Earth and Planetary Science Letters* 521, 60–67. https://doi.org/10.1016/j.epsl.2019.05.037

Pertermann, M., Hirschmann, M.M. (2003) Anhydrous Partial Melting Experiments on MORB-like Eclogite: Phase Relations, Phase Compositions and Mineral-Melt Partitioning of Major Elements at 2-3 GPa. *Journal of Petrology* 44, 2173–2201. https://doi.org/10.1093/petrology/egg074

Pertermann, M., Hirschmann, M.M., Hametner, K., Günther, D., Schmidt, M.W. (2004) Experimental determination of trace element partitioning between garnet and silica-rich liquid during anhydrous partial melting of MORB-like eclogite. *Geochemistry, Geophysics, Geosystems* 5, 2003GC000638. https://doi.org/10.1029/2003GC000638

Plank, T., Langmuir, C.H. (1998) The chemical composition of subducting sediment and its consequences for the crust and mantle. *Chemical Geology* 145, 325–394. https://doi.org/10.1016/S0009-2541(97)00150-2

Ringwood, A.E., Green, D.H. (1966) An experimental investigation of the Gabbro-Eclogite transformation and some geophysical implications. *Tectonophysics* 3, 383–427. https://doi.org/10.1016/0040-1951(66)90009-6

Salters, V.J.M., Longhi, J.E., Bizimis, M. (2002) Near mantle solidus trace element partitioning at pressures up to 3.4 GPa. *Geochemistry, Geophysics, Geosystems* 3, 1–23. https://doi.org/10.1029/2001GC000148

Salters, V.J.M., Stracke, A. (2004) Composition of the depleted mantle. *Geochemistry, Geophysics, Geosystems* 5, 2003GC000597. https://doi.org/10.1029/2003GC000597

Sobolev, A.V., Hofmann, A.W., Nikogosian, I.K. (2000) Recycled oceanic crust observed in 'ghost plagioclase' within the source of Mauna Loa lavas. *Nature* 404, 986–990. https://doi.org/10.1038/35010098

Sobolev, A.V., Hofmann, A.W., Sobolev, S.V., Nikogosian, I.K. (2005) An olivine-free mantle source of Hawaiian shield basalts. *Nature* 434, 590–597. https://doi.org/10.1038/nature03411

Soderman, C.R., Shorttle, O., Matthews, S., Williams, H.M. (2022) Global trends in novel stable isotopes in basalts: Theory and observations. *Geochimica et Cosmochimica Acta* 318, 388–414. https://doi.org/10.1016/j.gca.2021.12.008

Spier, C., Deoliveira, S., Sial, A., Rios, F. (2007) Geochemistry and genesis of the banded iron formations of the Cauê Formation, Quadrilátero Ferrífero, Minas Gerais, Brazil. *Precambrian Research* 152, 170–206. https://doi.org/10.1016/j.precamres.2006.10.003

Sun, S.-s., McDonough, W.F. (1989) Chemical and isotopic systematics of oceanic basalts: implications for mantle composition and processes. *Geological Society, London, Special Publications* 42, 313–345. https://doi.org/10.1144/GSL.SP.1989.042.01.19

Thomson, A.R., Walter, M.J., Kohn, S.C., Brooker, R.A. (2016) Slab melting as a barrier to deep carbon subduction. *Nature* 529, 76–79. https://doi.org/10.1038/nature16174

Tuff, J., Gibson, S.A. (2007) Trace-element partitioning between garnet, clinopyroxene and Fe-rich picritic melts at 3 to 7 GPa. *Contributions to Mineralogy and Petrology* 153, 369–387. https://doi.org/10.1007/s00410-006-0152-x

Walter, M.J. (1998) Melting of Garnet Peridotite and the Origin of Komatiite and Depleted Lithosphere. *Journal of Petrology* 39, 29–60. https://doi.org/10.1093/petroj/39.1.29

Wang, Y., He, Y., Wang, Z.-N., Lu, W.-N., Meng, X.-N., Zhu, C., Ke, S. (2023) High-Precision Calcium Isotope Analysis on TIMS Using A Double Spike Technique: The Instrumental Drift and Its Correction. *Atomic Spectroscopy* 44, 45–54. https://doi.org/10.46770/AS.2023.043

Wang, Y., He, Y., Wu, H., Zhu, C., Huang, S., Huang, J. (2019) Calcium isotope fractionation during crustal melting and magma differentiation: Granitoid and mineral-pair perspectives. *Geochimica et Cosmochimica Acta* 259, 37–52. https://doi.org/10.1016/j.gca.2019.05.030

Wang, Z.-N., Wang, Y., Sossi, P., He, Y., Peng, Y., Lu, W.-N., Wu, H. (2024) Calcium isotopic composition of the bulk silicate Earth: A komatiite perspective. *Lithos* 480–481, 107638. https://doi.org/10.1016/j.lithos.2024.107638

White, W.M., Klein, E.M. (2014) 4.13 - Composition of the Oceanic Crust. *Treatise on Geochemistry*. Elsevier, 457–496. https://doi.org/10.1016/B978-0-08-095975-7.00315-6

Williams, H.M., Bizimis, M. (2014) Iron isotope tracing of mantle heterogeneity within the source regions of oceanic basalts. *Earth and Planetary Science Letters* 404, 396–407. https://doi.org/10.1016/j.epsl.2014.07.033

Woodhead, J.D., Devey, C.W. (1993) Geochemistry of the Pitcairn seamounts, I: source character and temporal trends. *Earth and Planetary Science Letters* 116, 81–99. https://doi.org/10.1016/0012-821X(93)90046-C

Woodhead, J.D., Greenwood, P., Harmon, R.S., Stoffers, P. (1993) Oxygen isotope evidence for recycled crust in the source of EM-type ocean island basalts. *Nature* 362, 809–813. https://doi.org/10.1038/362809a0

Woodhead, J.D., McCulloch, M.T. (1989) Ancient seafloor signals in Pitcairn Island lavas and evidence for large amplitude, small length-scale mantle heterogeneities. *Earth and Planetary Science Letters* 94, 257–273. https://doi.org/10.1016/0012-821X(89)90145-3

Workman, R.K., Hart, S.R. (2005) Major and trace element composition of the depleted MORB mantle (DMM). *Earth and Planetary Science Letters* 231, 53–72. https://doi.org/10.1016/j.epsl.2004.12.005

Yaxley, G.M., Green, D.H. (1998) Reactions between eclogite and peridotite: Mantle refertilisation by subduction of oceanic crust. *Schweizerische mineralogische und petrographische Mitteilungen* 78, 243–255. petrographische Mitteilungen 78, 243-255.

Zhang, H., Wang, Y., He, Y., Teng, F., Jacobsen, S.B., Helz, R.T., Marsh, B.D., Huang, S. (2018) No Measurable Calcium Isotopic Fractionation During Crystallization of Kilauea Iki Lava Lake. *Geochemistry, Geophysics, Geosystems* 19, 3128–3139. https://doi.org/10.1029/2018GC007506

Zhu, H., Liu, F., Li, X., An, Y., Nan, X., Du, L., Huang, F., Sun, W., Zhang, Z. (2020) Significant $\delta^{44/40}$Ca variations between carbonate- and clay-rich marine sediments from the Lesser Antilles forearc and implications for mantle heterogeneity. *Geochimica et Cosmochimica Acta* 276, 239–257. https://doi.org/10.1016/j.gca.2020.02.033